Nonlinear Dynamics (2006) 45: 109–130
DOI: 10.1007/s11071-006-1856-1

Analysis of Thin Beams and Cables Using the Absolute Nodal Co-ordinate Formulation

JOHANNES GERSTMAYR[1,*] and AHMED A. SHABANA[2]
[1]*Institute for Technical Mechanics, Johannes Kepler University of Linz, Altenbergerstr. 69, 4040 Linz, Austria;* [2]*Department of Mechanical Engineering, University of Illinois at Chicago, 842 West Taylor Street, Chicago, IL 60607, U.S.A.;*
[*]*Author for correspondence (e-mail: johannes.gerstmayr@jku.at, tel.: +43 732 2468 9762; fax: +43 732 2468 9763)*

(Received: 8 April 2005; accepted: 25 July 2005)

Abstract. The purpose of this paper is to present formulations for beam elements based on the absolute nodal co-ordinate formulation that can be effectively and efficiently used in the case of thin structural applications. The numerically stiff behaviour resulting from shear terms in existing absolute nodal co-ordinate formulation beam elements that employ the continuum mechanics approach to formulate the elastic forces and the resulting locking phenomenon make these elements less attractive for slender stiff structures. In this investigation, additional shape functions are introduced for an existing spatial absolute nodal co-ordinate formulation beam element in order to obtain higher accuracy when the continuum mechanics approach is used to formulate the elastic forces. For thin structures where bending stiffness can be important in some applications, a lower order cable element is introduced and the performance of this cable element is evaluated by comparing it with existing formulations using several examples. Cables that experience low tension or catenary systems where bending stiffness has an effect on the wave propagation are examples in which the low order cable element can be used. The cable element, which does not have torsional stiffness, can be effectively used in many problems such as in the formulation of the sliding joints in applications such as the spatial pantograph/catenary systems. The numerical study presented in this paper shows that the use of existing implicit time integration methods enables the simulation of multibody systems with a moderate number of thin and stiff finite elements in reasonable CPU time.

Key words: absolute nodal co-ordinate formulation, flexible multibody system, sliding joint, thin elements

1. Introduction

Structural finite elements are widely used in flexible multibody simulations due to its ability to systematically model the body deformation. Problems of small deformation superimposed on a large rigid body motion led to the development of the well-known floating frame of reference approach [1]. While linear deformation models are important, some problems such as high speed rotating flexible beams motivated the development of models that include the effect of geometric or stress stiffening [2]. In the floating frame of reference approach, the mass matrix is not constant and the quadratic velocity dependent centrifugal and Coriolis forces are not equal to zero. On the other hand, the stiffness matrix is constant in the case of linear deformation models, while it is non-constant in the case of geometric or material non-linearities. The computational efficiency can be improved for systems with non-constant mass matrices by using implicit time integration methods and simplified Jacobians [3]. However, in the case of explicit integration, it is desirable to have a constant mass matrix whenever it is possible.

As an alternative to the floating frame of reference formulation, non-linear finite element methods, such as the absolute nodal co-ordinate formulation (ANCF), have been adopted for multibody system applications [1]. In the absolute nodal co-ordinate formulation, co-ordinates that consist of displacement

and gradient degrees of freedom at the nodal points are employed. A consistent mass formulation must be used and the gradients must be determined as derivatives of absolute position vectors. In the case of explicit time integration methods, a transformation to Cholesky co-ordinates is used in order to obtain an optimum sparse matrix formulation that is based on an identity generalized inertia matrix [4]. The use of this transformation makes the computational cost mainly dependent on the evaluation of the elastic forces. A co-rotational Jacobian matrix based on a reduced strain formulation was introduced for implicit integration schemes where the factorization of the Jacobian based on the absolute co-ordinates can be avoided at every time step, see Gerstmayr [5]. Several ANCF beam and plate elements were introduced, either using a continuum mechanics approach where the elastic forces are evaluated using a planar or spatial displacement field defined in terms of the nodal co-ordinates, or using classical beam and plate theories. The latter approach was introduced for two-dimensional elements when the absolute nodal co-ordinate formulation was first introduced [6].

Accurate dynamic modelling and efficient simulation of thin structural elements and cables in mechanical system applications is important and is now feasible after introducing the finite element absolute nodal co-ordinate formulation. Examples of such systems are the pantograph/catenary systems and marine cables. While in some cable problems the effect of bending stiffness can be neglected, the effect of the bending stiffness becomes important in the case of low tension as shown in Buckham et al. [7] or in high-speed pantograph/catenary applications [8]. Several authors examined the performance of the absolute nodal co-ordinate formulation and compared their results with the results of existing methods in the case of large deformation problems. While most authors considered examples with low Young's modulus and moderately thin cross-section [6, 9], the difficulties encountered in obtaining a solution for stiff thin structures, due to the Poisson locking phenomenon, are known and well documented in the literature [10]. Without making any correction and using a Poisson ratio different from zero, the numerical solution does not converge to the known analytical solutions by increasing the number of elements.

The objective of the study presented in this paper is to make improvements to the existing ANCF beam elements when such elements are used to model thin and stiff structural components in multibody system applications. It has been observed that for thin beams modelled by the original continuum-based ANCF, the solution converges slowly by increasing the number of elements compared to other beam elements that employ comparable third-order interpolation of the displacement of the beam centreline. The convergence problems depend on the aspect ratio and Young's modulus. The slow convergence is due to the fact that bending strain is constant over the length of the beam. The latter problem leads to significant errors in the deformation of very thin elements and is therefore addressed in the present study. Apart from torsion, the Poisson locking can be avoided for thin beams by setting the Poisson ratio to zero, otherwise, correction terms are needed as presented by Sopanen and Mikkola [10]. The high stiffness associated with some shear components also leads to very small time steps in the case of the explicit integration methods and slow Newton convergence in the case of implicit integration methods.

Two different methods for improving the convergence in the case of thin beam elements are proposed in this study. In the first method, the improvement is made by using additional shape functions. While the use of this method leads to 25% more degrees of freedom per element, it significantly improves the accuracy. In the second method, a reduced order element with a number of degrees of freedom smaller than the original formulation is used. The reduced order element has only 6 degrees of freedom for each node. The main problem, which can be less significant in many cable applications, is that this cable element in the straight undeformed configuration can not describe a rotation about its axis. This rotation, however, can be included for this element as shown in the work of Dmitrochenko and Pogorelov [11] at

the expense of adding algebraic equations and the possibility of having singular configurations due to lack of rotational inertia. The other alternative to introduce this rotation is to use the method proposed by Von Dombrowski at the expense of having a non-constant mass matrix [12]. As previously pointed out, pure torsional motion can be less significant in many thin beam or cable problems, and therefore, the new element can be effectively and efficiently used in these applications.

2. The Original Absolute Nodal Co-ordinate Formulation

In the following, we consider the three-dimensional ANCF beam element [13] which is denoted in this paper as the *original ANCF element*. The beam element has 24 degrees of freedom, 12 at each node. The vector $\mathbf{r}$ denotes the global position vector, in the deformed configuration, of an arbitrary point $\mathbf{x} = [\, x \;\; y \;\; z \,]^{\mathrm{T}}$. The vector of nodal co-ordinates consists of three position degrees of freedom and the following nine components of the position vector gradients:

$$\nabla \mathbf{r} = [\, \mathbf{r}_x \;\; \mathbf{r}_y \;\; \mathbf{r}_z \,]. \tag{1}$$

The derivatives of the position vector $\mathbf{r}$ with respect to co-ordinates x, y and z are denoted as

$$\mathbf{r}_x = \frac{\partial \mathbf{r}}{\partial x}, \quad \mathbf{r}_y = \frac{\partial \mathbf{r}}{\partial y}, \quad \mathbf{r}_z = \frac{\partial \mathbf{r}}{\partial z} \tag{2}$$

The co-ordinates of node j are represented as

$$\mathbf{e}_j = \left[\mathbf{r}^{\mathrm{T}} \quad \mathbf{r}_x^{\mathrm{T}} \quad \mathbf{r}_y^{\mathrm{T}} \quad \mathbf{r}_z^{\mathrm{T}} \right]^{\mathrm{T}} \tag{3}$$

and the element co-ordinates are denoted as

$$\mathbf{e} = \left[\mathbf{e}_1^{\mathrm{T}} \quad \mathbf{e}_2^{\mathrm{T}} \right]^{\mathrm{T}}. \tag{4}$$

The local positions of nodes 1 and 2 are given respectively

$$\mathbf{r}_{\text{node 1}} = \begin{bmatrix} x = 0 \\ y = 0 \\ z = 0 \end{bmatrix}, \quad \mathbf{r}_{\text{node 2}} = \begin{bmatrix} x = L \\ y = 0 \\ z = 0 \end{bmatrix}. \tag{5}$$

The finite element is based on a continuum mechanics approach, which means that the position vector $\mathbf{r}$ is function of the three spatial element parameters x, y and z, and is given by

$$\mathbf{r} = \begin{bmatrix} r_1 \\ r_2 \\ r_3 \end{bmatrix} = \begin{bmatrix} a_0 + a_1 x + a_2 y + a_3 z + a_4 xy + a_5 xz + a_6 x^2 + a_7 x^3 \\ b_0 + b_1 x + b_2 y + b_3 z + b_4 xy + b_5 xz + b_6 x^2 + b_7 x^3 \\ c_0 + c_1 x + c_2 y + c_3 z + c_4 xy + c_5 xz + c_6 x^2 + c_7 x^3 \end{bmatrix} \tag{6}$$

The position vector expressed in terms of the nodal co-ordinates is given by

$$\mathbf{r} = [\, S_1\mathbf{I} \quad S_2\mathbf{I} \quad S_3\mathbf{I} \quad S_4\mathbf{I} \quad S_5\mathbf{I} \quad S_6\mathbf{I} \quad S_7\mathbf{I} \quad S_8\mathbf{I} \,]\mathbf{e} \tag{7}$$

where $\mathbf{I}$ is a 3×3 identity matrix and the shape functions are defined as

$$\left.\begin{array}{ll} S_1 = 1 - 3\xi^2 + 2\xi^3, & S_2 = L(\xi - 2\xi^3 + \xi^3) \\ S_3 = L(1-\xi)\eta, & S_4 = L(1-\xi)\zeta \\ S_5 = 3\xi^2 - 2\xi^3, & S_6 = L(-\xi^2 + \xi^3) \\ S_7 = L\xi\eta, & S_8 = L\xi\zeta \end{array}\right\} \tag{8}$$

with $\xi = x/L$, $\eta = y/L$, and $\zeta = z/L$. The interpolation of displacements is cubic in x and linear in y- and z-direction. Constant terms are sufficient to describe rigid-body translations and linear terms in x, y and z can describe exact rigid body rotations without approximations in the inertia terms. The modelling is different from existing non-linear finite beam elements, such as the elements proposed by Simo and Vu-Quoc [14], and Bathe [15] which are based on beam kinematics.

3. Absolute Nodal Co-ordinate Formulation Extended to Thin Beams

Locking effects can arise when low order interpolation functions are used or incompatibilities in the interpolation functions with respect to deformation of the axis and representation of axial strain in the cross-section are present. Locking is commonly used to describe the phenomenon that arises when the approximate stiffness of an element is much larger than the exact value, and such stiffness is dependent on a certain parameter such as the thickness of the element. A general analysis of locking effects is given by Braess [16] who showed that locking is commonly related to poorly conditioned problems. This section discusses an extension of the original ANCF element by means of adding shape functions. The basic idea becomes clear after examination of the *modes* of the original ANCF. Figure 1 shows the first 12 modes, which are generated by using the following initial values for the element nodal co-ordinates:

$$\mathbf{e}_0 = \left[\begin{bmatrix} 0 \\ 0 \\ 0 \end{bmatrix}^{\mathrm{T}} \begin{bmatrix} 1 \\ 0 \\ 0 \end{bmatrix}^{\mathrm{T}} \begin{bmatrix} 0 \\ 1 \\ 0 \end{bmatrix}^{\mathrm{T}} \begin{bmatrix} 0 \\ 0 \\ 1 \end{bmatrix}^{\mathrm{T}} \begin{bmatrix} 1 \\ 0 \\ 0 \end{bmatrix}^{\mathrm{T}} \begin{bmatrix} 1 \\ 0 \\ 0 \end{bmatrix}^{\mathrm{T}} \begin{bmatrix} 0 \\ 1 \\ 0 \end{bmatrix}^{\mathrm{T}} \begin{bmatrix} 0 \\ 0 \\ 1 \end{bmatrix}^{\mathrm{T}} \right]^{\mathrm{T}}. \tag{9}$$

This equation shows the nodal co-ordinates of one element according to Equations (3) and (4) assuming a unit-length and assuming that the element is straight and its axis is parallel to the X-axis. The shapes presented in Figure 1 are obtained by giving a small perturbation to the ith element in the vector of nodal co-ordinates. Modes 13–24 are similar to Modes 1–12 except that the right node shows deformation and the left node is at rest. The interpretation of the modes depends on the initial configuration, given here by Equation (9) and is discussed later.

Modes 1 and 4 represent linear and quadratic axial deformations. Modes 2, 3, 5 and 6 correspond to bending of the axis. Modes 7 and 10 allow representation of the deformation in the special case of a Bernoulli–Euler beam in which the cross-section remains perpendicular to the beam centreline. However, this special case can be only fulfilled approximately, because Modes 7 and 10 are linear, while the bending modes are cubic. Using these shapes, the locking effect is discussed later. For large deformation, Modes 8 and 12 in combination with shear Modes 7 and 10 contribute to the change in dimensions of the cross-section. Torsion is represented by Modes 9 and 11 together with Modes 8 and 12. In fact, Modes 2, 3, 5 and 6 represent only shear deformation and in combination with axial deformation Modes 7 and 10 beam-like behaviour can be represented.

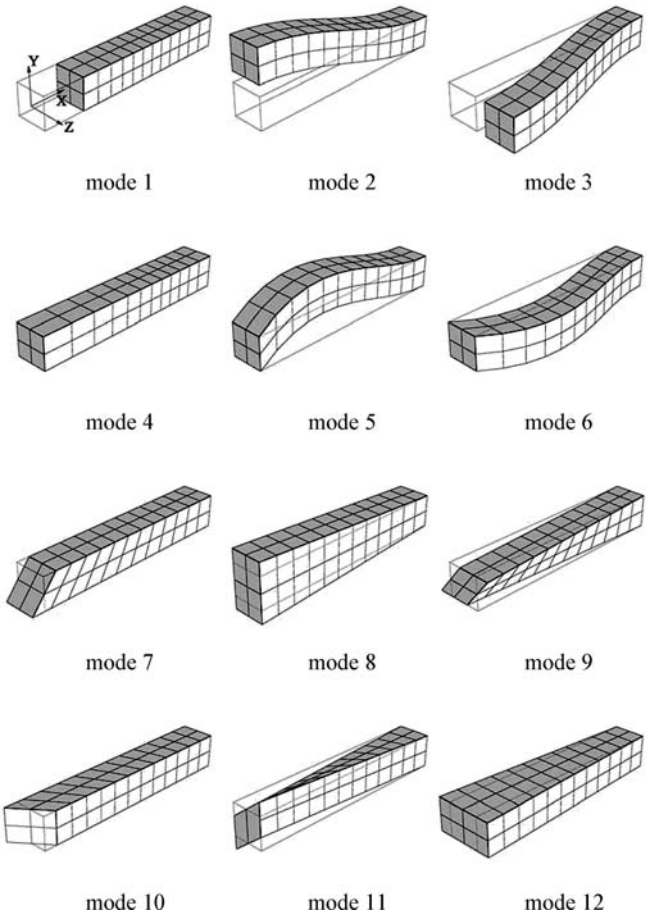

Figure 1. Modes 1–12 for the original ANCF two-node beam element.

In the case of very thin beams, it can be assumed that the displacement field will be almost as in the Bernoulli–Euler beam, which means that the cross-section remains perpendicular to the axis and that there is no shear deformation. A detailed discussion on the kinematical relations of the absolute nodal co-ordinate formulation beam element compared to Bernoulli–Euler and Reissner's beam models has been provided by Sugiyama et al. [17]. In order to further investigate locking effects, small deformation is assumed in the remaining part of this section. The axial strain field ε_{xx} is related linearly to the curvature approximated by the second derivatives of the deflection w in z-direction and v in y-direction,

$$\varepsilon_{xx} = -z w_{xx} - y v_{xx} + u_x, \tag{10}$$

Here, z and y are local co-ordinates of the beam cross-section, w is the deflection in the z-direction, v is the deflection in the y-direction and u is the axial deformation. In the case of small deformation of an ANCF element, the derivatives in the preceding equation defined at a point located on the beam centreline can be approximated as

$$w_{xx} = \frac{\partial^2 r_3}{\partial x^2} = 2c_6 + 6c_7 x, \quad v_{xx} = \frac{\partial^2 r_2}{\partial x^2} = 2b_6 + 6b_7 x. \tag{11}$$

It follows that w_{xx} and v_{xx} are linear functions in x. However, the strain field computed from Equation (6) in the linear case can be written as

$$\varepsilon_{xx} = \frac{\partial r_1}{\partial x} = a_1 + a_4 y + a_5 z + 2a_6 x + 3a_7 x^2. \tag{12}$$

This expression can be written as the sum of two components; one related to axial deformation ($\varepsilon^{\mathrm{a}}_{xx}$) and the other related to bending ($\varepsilon^{\mathrm{b}}_{xx}$), that is

$$\varepsilon^{\mathrm{a}}_{xx} = a_1 + 2a_6 x + 3a_7 x^2, \quad \varepsilon^{\mathrm{b}}_{xx} = a_4 y + a_5 z. \tag{13}$$

Note that the strain due to bending is linear in x, if it is calculated from Equation (11) and substituted into Equation (10). The original ANCF element, however, does not lead to the same result if the continuum mechanics approach is used. Instead, one obtains Equation (13), which shows that $\varepsilon^{\mathrm{b}}_{xx}$ does not depend on x. This lower order representation of the bending strain, as compared to Equation (10), eliminates possible deformation modes and leads to an artificial numerically induced bending stiffness of the beam element, which is interpreted as shear locking for the case described earlier. Note, that due to incompatibilities in the shape functions, the special case of a cross-section that has dimension independent of x, as in the case of the Bernoulli–Euler beam, cannot be described. This results in more severe thickness locking (which is different from Poisson locking and might also occur in the case of zero Poisson ratio). Both locking effects appear coupled in the numerical examples and are not separately investigated.

It is, therefore, important to investigate the locking problem in order to avoid the numerical difficulties encountered when the original three-dimensional ANCF beam element is used. In order to solve this problem, one may attempt to change the shape functions in Equation (8) by including higher order polynomials in the assumed displacement field. Alternatively, two other solutions to circumvent this problem are proposed in this study; one possibility is to introduce a higher order element; while in the second solution, a lower order element is used.

4. Higher Order Element

First, the case of a higher order element is considered. In this case, additional shape functions that produce not only linear interpolation for w_{xx} and v_{xx} but also linear interpolation in x for the strain $\varepsilon^{\mathrm{b}}_{xx}$ is introduced. The new interpolation polynomials are given by

$$\mathbf{r} = \begin{bmatrix} r_1 \\ r_2 \\ r_3 \end{bmatrix} = \begin{bmatrix} a_0 + a_1 x + a_2 y + a_3 z + a_4 xy + a_5 xz + a_6 x^2 + a_7 x^3 + a_8 x^2 y + a_9 x^2 z \\ b_0 + b_1 x + b_2 y + b_3 z + b_4 xy + b_5 xz + b_6 x^2 + b_7 x^3 + b_8 x^2 y + b_9 x^2 z \\ c_0 + c_1 x + c_2 y + c_3 z + c_4 xy + c_5 xz + c_6 x^2 + c_7 x^3 + c_8 x^2 y + c_9 x^2 z \end{bmatrix}. \tag{14}$$

where new y- and z-dependent functions that are quadratic in x have been added. While this leads to 25% increase in the number of degrees of freedom, significant improvement in accuracy can be obtained as demonstrated by the results presented in Section 7. As alternatives, enhanced assumed strain (EAS) concepts can be used to reduce locking effects without increasing the number of co-ordinates [18]. The use of the enhanced strain concepts can be the subject of future investigations in this area. Recently, Schwab and Meijaard [24] have shown locking effects in the ANCF elements and successfully applied the elastic line concept to avoid locking.

The co-ordinates for the new element are

$$\mathbf{e} = \left[\mathbf{e}_1^{\mathrm{T}} \quad \mathbf{e}_2^{\mathrm{T}} \quad \mathbf{r}_{yx}^{\mathrm{T}}\big|_{x=0} \quad \mathbf{r}_{zx}^{\mathrm{T}}\big|_{x=0} \right]^{\mathrm{T}} \tag{15}$$

which consist of nodal co-ordinates $[\,\mathbf{e}_1^{\mathrm{T}} \quad \mathbf{e}_2^{\mathrm{T}}\,]^{\mathrm{T}}$ and internal co-ordinates $[\,\mathbf{r}_{yx}^{\mathrm{T}}|_{x=0}\ \mathbf{r}_{zx}^{\mathrm{T}}|_{x=0}\,]$. The nodal co-ordinates are still the same as in the original element and the new element does not lead to continuous derivatives $\mathbf{r}_{yx}$ and $\mathbf{r}_{zx}$ at the interface. Other geometrical representation of the new co-ordinates can be chosen, such as $\mathbf{r}_{yx}$ and $\mathbf{r}_{zx}$ at $x = L$.

The new degrees of freedom can be geometrically interpreted as the change over x of the gradients $\mathbf{r}_y$ and $\mathbf{r}_z$, which define the beam cross-section. In the original element, discussed in the preceding section, see Equation (6), these gradients may only vary linearly over the length of the element. In the new element, the gradients $\mathbf{r}_y$ and $\mathbf{r}_z$ vary as quadratic functions over the length, which leads to better performance of the element, particularly in the case of large deformation. At the boundary, the derivatives of the gradients with respect to x are not constrained, and connectivity conditions are applied only to the gradients as in the case of the original ANCF element. Thus, the new shape functions lead to the same boundary conditions as in the original element. Compared to Equation (7), the global position vector for the new element can be written as

$$\mathbf{r} = [\, S_1\mathbf{I}\ S_2\mathbf{I}\ S_3\mathbf{I}\ S_4\mathbf{I}\ S_5\mathbf{I}\ S_6\mathbf{I}\ S_7\mathbf{I}\ S_8\mathbf{I}\ S_9\mathbf{I}\ S_{10}\mathbf{I}\,]\mathbf{e}. \tag{16}$$

where the shape functions are given by

$$\left.\begin{array}{ll} S_1 = 1 - 3\xi^2 + 2\xi^3, & S_2 = L(\xi - 2\xi^3 + \xi^3), \\ S_3 = L(1 - \xi^2)\eta, & S_4 = L(1 - \xi^2)\zeta, \\ S_5 = 3\xi^2 - 2\xi^3, & S_6 = L(-\xi^2 + \xi^3), \\ S_7 = L\xi^2\eta, & S_8 = L\xi^2\zeta, \\ S_9 = (\xi - \xi^2)L^2\eta, & S_{10} = (\xi - \xi^2)L^2\zeta. \end{array}\right\} \tag{17}$$

Definitions of mass matrix, elastic forces, external forces or constraint conditions can be made as in the case of the original beam element [13]. As shown in Section 7, the locking problem can be avoided by introducing the additional shape functions. Furthermore, the convergence is improved for large deformation problems and the rate of convergence is comparable to a third order element based on the beam theory.

5. Lower Order Cable Element

While the introduction of additional shape functions contributes to solving the problem of locking in the cases of small and large deformation problems, the very stiff components of the shear modes remain in the equations of motion and can make the element inefficient, as demonstrated in Section 7. Therefore, a lower order cable element that is based on the absolute nodal co-ordinate formulation is discussed in this section. For this element, one position vector and only one gradient vector obtained by differentiation with respect to x are used as the co-ordinates for each node. Note that with this selection of co-ordinates, this cable element cannot describe a rotation of a beam about its axis. While it is possible to model bending effects, the element is not suitable for pure torsional effects.

The cable element is similar to the element developed by Von Dombrowski [12] who included torsional effects at the expense of having a non-constant mass matrix, and Dmitrochenko and Pogorelov [11] who used additional algebraic variables for the description of the rotation about the beam axis at the nodal points. The latter approach leads to singularities in the case of rotations about the undeformed axis of a beam and should be used carefully. However, as will be shown by numerical examples, in many three-dimensional problems torsional stiffness does not have a significant effect. The cable element has the advantage that it has only half of the degrees of freedom as the original ANCF element and it has no stiff terms related to shear deformation.

The nodal co-ordinates at $x = 0$ and $x = L$ of the cable element are defined as

$$\mathbf{e}_j = \begin{bmatrix} \mathbf{r}^{\mathrm{T}} & \mathbf{r}_x^{\mathrm{T}} \end{bmatrix}^{\mathrm{T}} \tag{18}$$

and the element co-ordinates are

$$\mathbf{e} = \begin{bmatrix} \mathbf{e}_1^{\mathrm{T}} & \mathbf{e}_2^{\mathrm{T}} \end{bmatrix}^{\mathrm{T}}. \tag{19}$$

The position of a point on the beam centreline at x in the undeformed configuration is given by

$$\mathbf{r} = \begin{bmatrix} r_1 \\ r_2 \\ r_3 \end{bmatrix} = \begin{bmatrix} a_0 + a_1 x + a_2 x^2 + a_3 x^3 \\ b_0 + b_1 x + b_2 x^2 + b_3 x^3 \\ c_0 + c_1 x + c_2 x^2 + c_3 x^3 \end{bmatrix}. \tag{20}$$

Note that this displacement field is written in terms of cubic polynomials in x. Axial and bending deformations in thin beams are, therefore, of the same order as in the original element. For this element, the displacement field can be written as

$$\mathbf{r} = \begin{bmatrix} S_1\mathbf{I} & S_2\mathbf{I} & S_3\mathbf{I} & S_4\mathbf{I} \end{bmatrix} \begin{bmatrix} \mathbf{e}_1^{\mathrm{T}} & \mathbf{e}_2^{\mathrm{T}} \end{bmatrix}^{\mathrm{T}} = \mathbf{S} \begin{bmatrix} \mathbf{e}_1^{\mathrm{T}} & \mathbf{e}_2^{\mathrm{T}} \end{bmatrix}^{\mathrm{T}}. \tag{21}$$

The shape functions in this equation are given by

$$\left.\begin{array}{ll} S_1 = \frac{1}{2} - \frac{3}{4}\xi + \frac{\xi^3}{4}, & S_2 = \frac{L}{8}(1 - \xi - \xi^2 + \xi^3), \\ S_3 = \frac{1}{2} + \frac{3}{4}\xi - \frac{\xi^3}{4}, & S_4 = \frac{L}{8}(-1 - \xi + \xi^2 + \xi^3) \end{array}\right\} \tag{22}$$

with the normalization $\xi = 2\frac{x}{L} - 1$. The mass matrix can be computed using integration with respect to x as

$$\mathbf{M} = A \int_0^L \rho \mathbf{S}^{\mathrm{T}} \mathbf{S}\, dx \tag{23}$$

where A is the cross-section area, L the length and ρ the density of the cable element.

The computation of the elastic forces (from the virtual work of internal forces) is split into two parts; a part due to bending based on the curvature of the deformed beam centreline, and a part due to the axial strain. Equal flexural rigidity with respect to both y- and z-axis is assumed in this investigation, that is

$$EI_{zz} = EI_{yy}. \tag{24}$$

The axial strain can be defined using the Green strain tensor as

$$\varepsilon_{xx}^{\mathrm{a}} = \frac{1}{2}\left(\mathbf{r}_x^{\mathrm{T}}\mathbf{r}_x - 1\right). \tag{25}$$

The curvature κ of the beam centreline is given by the formula for the curvature related to an arbitrary parameter [19],

$$\kappa = \frac{|\mathbf{r}_x \times \mathbf{r}_{xx}|}{|\mathbf{r}_x|^3}. \tag{26}$$

This formula can be derived from the Seret–Frenet frame, see Appendix A. Using the well-known Bernoulli–Euler beam formulation, the virtual work of internal forces can be written as

$$\delta W = \int_0^L EI\kappa\delta\kappa + EA\varepsilon_{xx}^{\mathrm{a}}\delta\varepsilon_{xx}^{\mathrm{a}}\, dx. \tag{27}$$

In the computer implementation, it is either possible to derive the expressions for the variations in Equation (27) by means of a symbolic computer program, or to derive them analytically in order to minimize the number of mathematical operations. Closed form expressions can be found in Appendix B. While Gaussian quadrature is used for exact integration of the mass matrix, the non-rational expressions of the integral in Equation (27) are approximated. It was found that five integration points for the axial strain components and three integration points for the curvature (bending) components are sufficient for accurate approximations of the elastic forces.

6. Sliding Joint

The formulation of the sliding joint in the absolute nodal co-ordinate formulation was introduced by Sugiyama et al. [20]. In this formulation, the second time derivative of the arc length was used. However, in implicit time integration, the equations for the sliding joint can be formulated differently. We start with the sliding joint constraint equations at the position level, leading to an index 3 formulation and derive an index 2 formulation by means of differentiation. An index 2 formulation together with stabilization techniques (GGL) is frequently used for implicit integration methods.

In the implicit integration based numerical algorithm used in this paper, the sliding joint is formulated using four constraint equations expressed in terms of three Lagrange multipliers and one non-generalized degree of freedom that represents the arc length parameter s. In the simple sliding joint, it is assumed that a fixed point $\mathbf{x}^i$ of the flexible or rigid body i is sliding along the centreline of a beam denoted as body j which can be a flexible or rigid element. The local (undeformed) positions of the sliding point on body i and j are given, respectively, by

$$\mathbf{x}^i = \begin{pmatrix} x_1^i \\ x_2^i \\ x_3^i \end{pmatrix}, \quad \mathbf{x}^j = \begin{pmatrix} x_1^j = s \\ x_2^j \\ x_3^j \end{pmatrix}. \tag{28}$$

The following constraint equations must be fulfilled for the sliding joint,

$$\mathbf{C} = \begin{bmatrix} \mathbf{r}^i(\mathbf{x}^i) - \mathbf{r}^j(\mathbf{x}^j) \\ \frac{\partial \mathbf{r}^j(\mathbf{x}^j)}{\partial x_1^j} \cdot \boldsymbol{\lambda} \end{bmatrix} = \mathbf{0}. \tag{29}$$

In Equation (29), the first three constraints are used to restrict the motion of the sliding point on body i and j to be at the same global position. This leads to three Lagrange multipliers $\boldsymbol{\lambda} = [\,\lambda_1 \;\; \lambda_2 \;\; \lambda_3\,]^{\mathrm{T}}$ associated with the constraint forces applied to both bodies. The vector of Lagrange multipliers must be perpendicular to the sliding direction, which means that in the friction-free case there is no force acting in the sliding direction. This is satisfied by means of the last equation line in Equation (29).

The non-generalized co-ordinate of the sliding joint can be systematically eliminated. As an example, one can determine the sliding parameter s by using the following equation:

$$(\mathbf{r}^i(\mathbf{x}^i) - \mathbf{r}^j(\mathbf{x}^j))\frac{\partial \mathbf{r}^j(\mathbf{x}^j)}{\partial x_1^j} = 0. \tag{30}$$

This equation constrains the points of the two bodies in the sliding direction, and therefore, results only in one equation which is of order 5 in s and which could be solved for the sliding parameter s by means of the Newton method. However, the remaining two position level constraints can be redefined by projection of the first three equations in Equation (29) along the normal and binormal of the Seret–Frenet frame. Since this approach can lead to a problem if the beam is straight (zero curvature), the sliding joint is formulated in this investigation using four equations without eliminating the non-generalized arc length parameter.

The formulation of the sliding joint in Equation (29) has index 3, and consequently, it can only be solved by means of advanced implicit integration techniques (such as RadauIIA 2 stage). One possible transformation to an index 2 formulation is shown in this section. We differentiate the position level equations with respect to time, keeping in mind that the sliding parameter (arc length s) is a function of time. The index 2 constraint equations for the sliding joint can be written as

$$\mathbf{C}_2 = \begin{bmatrix} \frac{\partial \mathbf{r}^i(\mathbf{x}^i)}{\partial t} - \frac{\partial \mathbf{r}^j(\mathbf{x}^j)}{\partial t} - \frac{\partial \mathbf{r}^j(\mathbf{x}^j)}{\partial x_1^j}\dot{s} \\ \frac{\partial \mathbf{r}^j(\mathbf{x}^j)}{\partial x_1^j} \cdot \boldsymbol{\lambda} \end{bmatrix} = \mathbf{0}. \tag{31}$$

The use of partial derivatives with respect to time shows the explicit dependence on the sliding velocity in Equation (31). The fourth constraint equation, $\frac{\partial \mathbf{r}^j(\mathbf{x}^j)}{\partial x_1^j} \cdot \boldsymbol{\lambda} = 0$, is not a position constraint that introduces Lagrange multipliers, and therefore it is not differentiated with respect to time. In order to show that Equation (31) is indeed of index 2, the first three constraints are differentiated once more with respect to time in order to obtain the following index 1 formulation:

$$\mathbf{C}_1 = \begin{bmatrix} \frac{\partial^2 \mathbf{r}^i(\mathbf{x}^i)}{\partial t^2} - \frac{\partial^2 \mathbf{r}^j(\mathbf{x}^j)}{\partial t^2} - 2\frac{\partial^2 \mathbf{r}^j(\mathbf{x}^j)}{\partial t\, \partial x_1^j}\dot{s} - \frac{\partial \mathbf{r}^j(\mathbf{x}^j)}{\partial x_1^j}\ddot{s} \\ \frac{\partial \mathbf{r}^j(\mathbf{x}^j)}{\partial x_1^j} \cdot \boldsymbol{\lambda} \end{bmatrix} = \mathbf{0}. \tag{32}$$

The acceleration terms in Equation (32) depend linearly on Lagrange multipliers $\boldsymbol{\lambda}$ through the equations of motion, and therefore, the constraints written in Equation (32) are of index 1.

7. Numerical Examples

The following numerical examples are used to demonstrate the problems encountered when using the original ANCF element (*ANCF original*) and the improvement of performance gained by using the proposed new locking-free element (*ANCF non-locking*) and the reduced order *cable element*. Different examples are used to show the performance and good convergence characteristics of the cable element despite the fact that such an element cannot describe rotation about its axis. An example of a three-dimensional pantograph/catenary system shows the range of applications of the cable element. The trapezoidal rule, which has been implemented in a time integration code called HOTINT, is used for all examples and the step size is chosen such that no significant error in the time integration is included in the presented results.

7.1. Example 1: Cantilever Beam

In order to investigate the convergence of the elements discussed in this investigation, a planar cantilever beam is studied. The beam has length 1 m, square cross-section area of $10^{-4} f^2\,\mathrm{m}^2$, mass density $\rho = 500/f^2\,\mathrm{kg/m}^3$, Young's modulus $E = 10^8/f^4\,\mathrm{N/m}^2$, zero Poisson ratio and f is a parameter that can be varied. The beam is subjected to its own load under gravity $g = 9.81\,\mathrm{m/s}^2$. The simulation is performed for 0.4 s with a step size of 0.25 ms and with $f = 1$. Large deformation occurs and the tip displacement in vertical direction at time $t = 0.4\,\mathrm{s}$ is measured and depicted in Figure 2, where different models and different numbers of elements are investigated. The new models for thin elements converge fast, while the original element converges slowly as the number of elements increases.

In Figure 3, the numerical behaviour of the implicit time integration measured by the number of necessary Jacobian evaluations, which represent a significant part of the computational costs in the time integration, is shown. The results presented in this figure are obtained using four elements. The number of Jacobian evaluations is plotted versus Young's modulus E, where the parameter f is varied

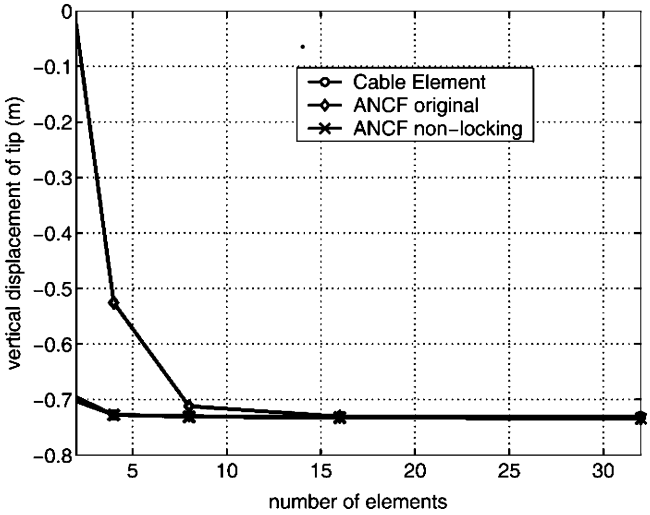

Figure 2. Comparison of vertical displacement of the tip of the cantilever beam at $t = 0.4\,\mathrm{s}$.

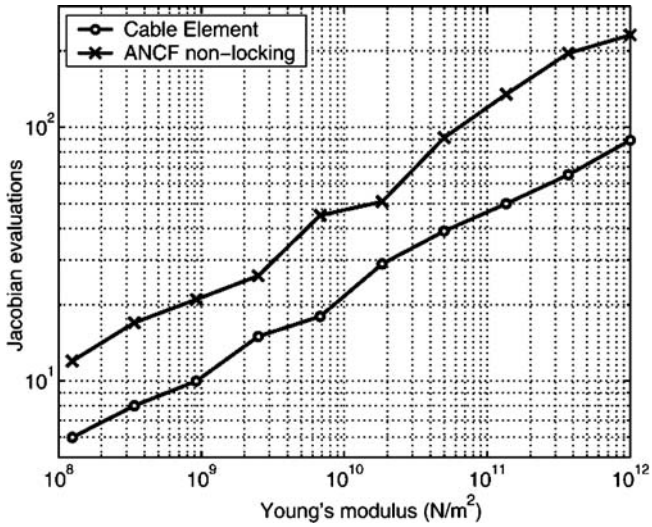

Figure 3. Number of Jacobian evaluations in implicit integration versus Young's modulus.

in the range 0.1–1. The bending stiffness and the load per unit length are kept constant, leading to approximately the same solution in the range $0.1 < f < 1$, but to a very different numerical behaviour. Figure 3 shows that both investigated models depend strongly on the stiffness parameters, while the cable element performs slightly better. The original ANCF element is not included in this comparison, since the change of f would also require increasing the number of elements in order to obtain the correct solution.

7.2. Three-Dimensional Pendulum Example

The second example is used to compare the performance of the three element models in the case of three-dimensional motion. An initially straight and horizontal three-dimensional pendulum is studied. The initial angular velocity of the pendulum about the vertical Y-axis is 4 rad/s. The parameter-dependent dimensions of the pendulum are length 1 m, cross-section area $10^{-6} f^2\,\mathrm{m}^2$, density $8000/f^2\,\mathrm{kg/m}^3$ and Young's modulus $10^9/f^4\,\mathrm{N/m}^2$. Poisson's ratio is assumed to be zero and the effect of gravity (z-direction) is considered. In the elements that include torsional effects, a constraint is added to prevent the rotation about the axis of the beam. The first study is performed with $f = 5$ and a step size of 0.1 ms for 2 s of simulation time. Only 4 elements are used for all the three models, while a 32 element reference solution based on the original ANCF element was obtained. Figure 4 shows the Z versus X position of the tip of the pendulum, starting at $X = 1$, $Y = 0$ and $Z = 0$. Figure 5 shows the Y position of the mid-point versus time for the same simulation. Both figures show converged reference solution with good agreements for the new elements, while the original element shows a considerably larger error. In another study, presented in Figure 6, the number of Jacobian updates as function of Young's modulus as result of changing the parameter f from 0.1 to 10 is plotted. The simulation with four elements runs for 0.5 s with step size 0.1 ms. While it is not possible to perform computations with Young's modulus higher than $10^9\,\mathrm{N/m}^2$ with the continuum-based elements in reasonable time because the Jacobian needs to be updated at every iteration, the cable element performs much better for a very high stiffness. For low stiffness, only one Jacobian update is needed for the whole simulation

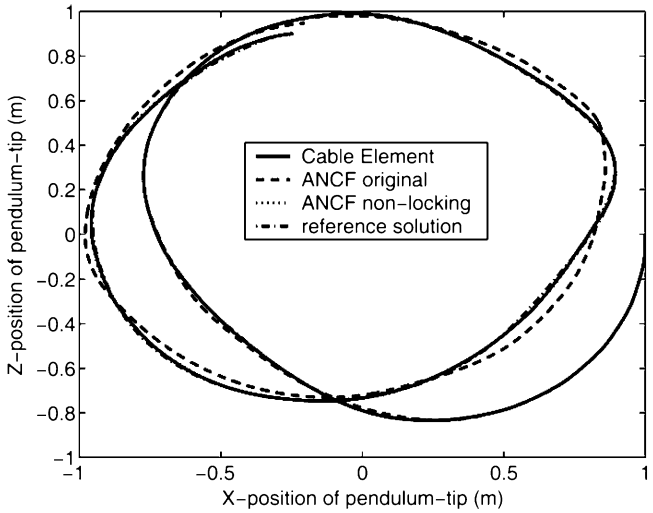

Figure 4. Plot of the Z versus X co-ordinate of the mid-point of the three-dimensional pendulum.

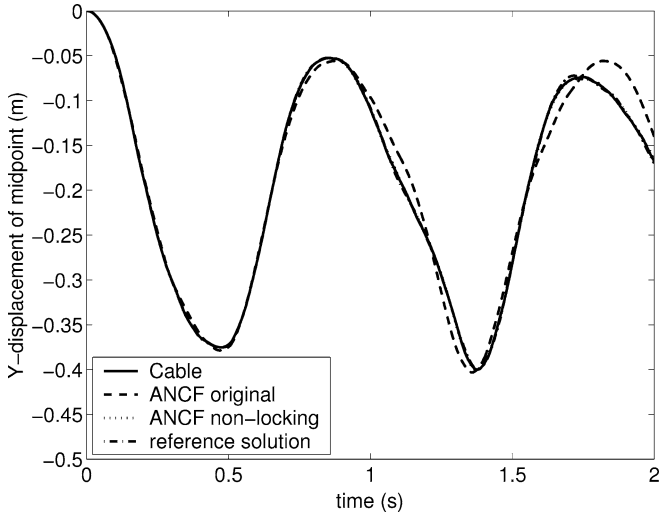

Figure 5. Y-displacement of the mid-point of the three-dimensional pendulum as function of time.

with the cable element, which shows that this element will also work well with explicit integration methods.

7.3. Spin-Up Maneuver

In order to investigate the geometric stiffening problem and in order to verify the implemented algorithms, results for the well-known spin-up of a rotating cantilever beam [21] are obtained. The parameters of the model are rectangular cross-section with $A = 7.299\,\text{e-}5\ \text{m}^2$, area moment of inertia $I = 8.215\,\text{e-}9\ \text{m}^4$, length $L = 8\,\text{m}$, Young's modulus $E = 68.95\,\text{e}9\ \text{N/m}^2$ and density $\rho = 2766.67\,\text{kg/m}^2$. The

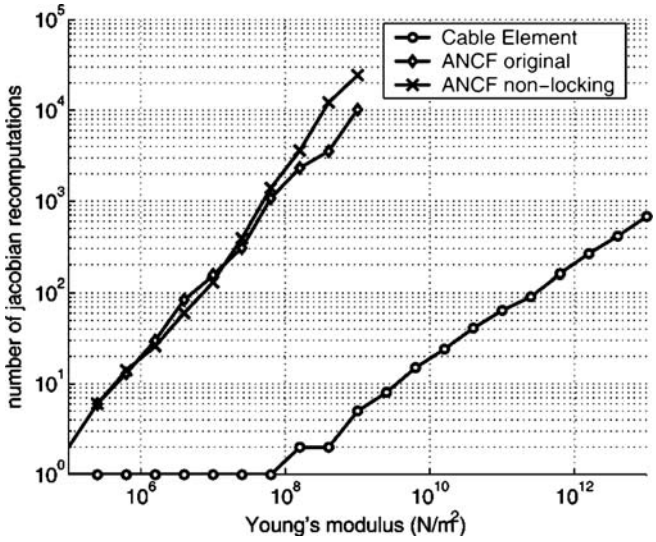

Figure 6. Number of Jacobian updates in implicit integration versus Young's modulus.

angular velocity that is prescribed at the support is given by

$$\theta(T) = \begin{cases} \left(\frac{\omega_s}{T_s}\right)\left[\left(\frac{t^2}{2}\right) + \left(\frac{T_s}{2\pi}\right)\left(\cos\left(\frac{2\pi t}{T_s}\right) - 1\right)\right] & 0 \le t \le T_s \\ \omega_s\left(t - \frac{T_s}{2}\right) & t > T_s \end{cases} \tag{33}$$

with $T_s = 15\,\text{s}$ and $\omega_s = 4\,\text{rad/s}$. The simulation is performed for 20 s with a step size of 1 ms. The in-plane tip displacement is measured with respect to a tangential frame attached to the support of the cantilever beam. Figure 7 shows the convergence of the tip displacement at time $t = 7\,\text{s}$ using different number of elements. The results presented in this figure show a better performance for the new elements.

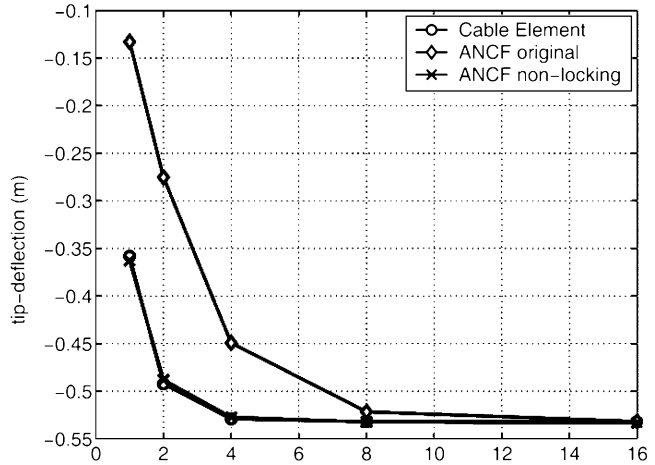

Figure 7. Convergence of the tip displacement in the rotating beam at $t = 7\,\text{s}$ using different formulations.

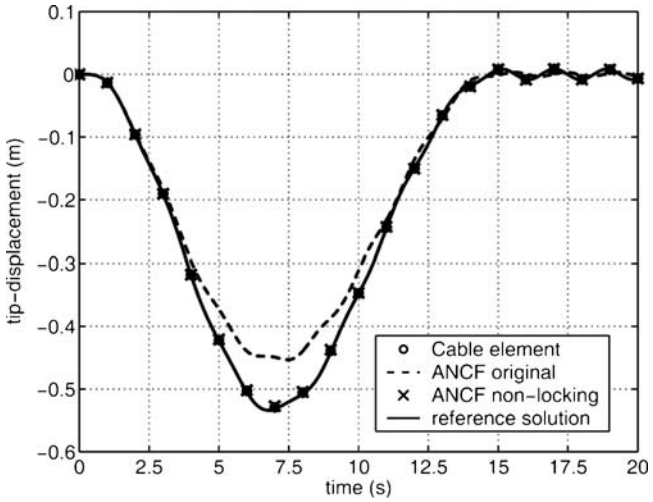

Figure 8. Tip displacement of the rotating beam using four elements and compared to a reference solution.

Figure 8 shows the tip displacement as function of time for a discretization of four elements for the three different models, while 16 elements of the original ANCF are used for the reference solution.

7.4. Sliding Three-Dimensional Beam with Eccentricity

A three-dimensional problem with a flexible beam sliding along another flexible beam has been presented by Sugiyama et al. [20] and studied by Muñoz and Jelenić [22]. In both referenced papers, only a discretization of one element per beam was used and the convergence of the solution was not investigated. The data of the model shown in Figure 9 are provided in Table 1. The carrier beam is hinged with two spherical joints, while one end of the sliding beam slides along the axis of the carrier beam. The tip of the sliding beam contains a point mass as shown in Figure 9. The sliding beam is initially straight and horizontal, while the carrier beam is initially in static equilibrium under the effect of gravity.

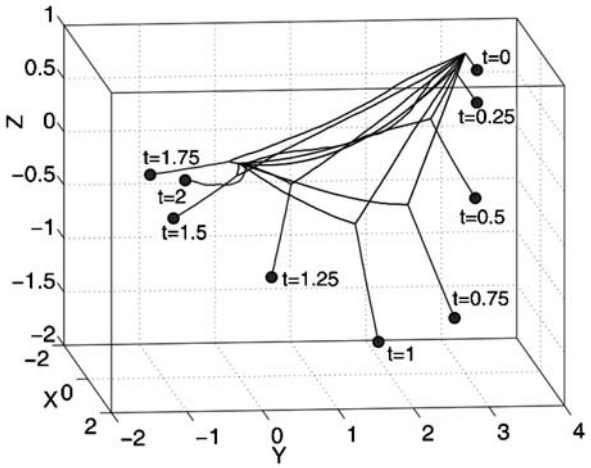

Figure 9. Configurations of the sliding three-dimensional beam example with 128+8 elements.

Table 1. Parameters for the sliding beam with eccentricity.

Initial position	Carrier beam	[0,0,0] – [0,3,1]
Initial position	Sliding beam	[0,3,1] – [1,3,1]
Initial position	Tip mass	[1,3,1]
Young's modulus	All	10^6 N/m^2
Mass density	All	800 kg/m^3
Cross-section	Square, both beams	10^{-4} m^2
Bending stiffness	Both axes	1/1200 Nm^2
Poisson coefficient	Not used for cable element	0.3
Tip mass	Of sliding beam	1 kg
Gravity	All	9.81 m/s^2

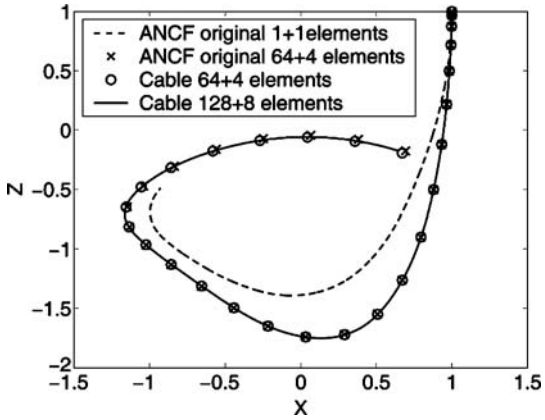

Figure 10. *X–Z* trajectory of the mass in the three-dimensional beam example.

A three-dimensional view of several configurations during simulation depicted in Figure 9 shows the slenderness of the cable, and therefore, the need for a larger number of elements compared to the number previously used in the literature. Converged results are obtained by 128+8 cable elements (carrier + sliding beam) and compared to 64+4 cable elements and the original ANCF element. Figures 10 and 11 show the position of the tip mass of the sliding beam in the *Z–X* and *Z–Y* plane, respectively. Table 2 shows simulation times using different numbers of elements for various models with 0.2 ms step size and 1 s of simulation time. While the higher order element usually takes more time than the original element, the lower order cable element leads to significantly reduced computational times even for higher number of elements.

Table 2. CPU time for different models (1 s simulation).

Model	No. of elements carrier+slider	Computational time (s)
ANCF original	6+2	38
ANCF non-locking	6+2	72
Cable element	6+2	6
Cable element	64+4	71

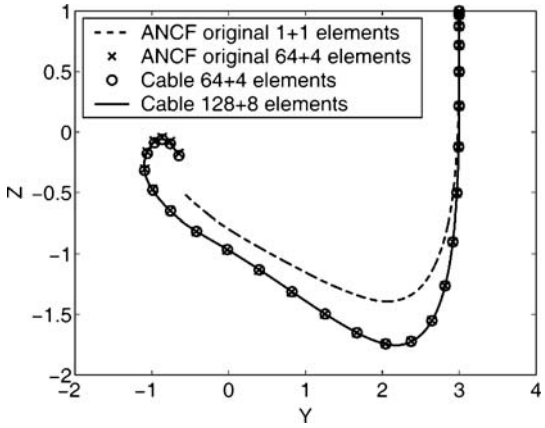

Figure 11. *Y–Z* trajectory of the mass in the three-dimensional beam example.

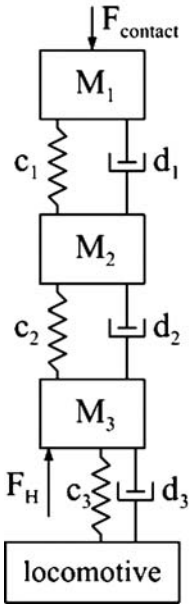

Figure 12. Sketch of the linear pantograph model.

7.5. Three-Dimensional Pantograph/Catenary System

The last example is used to demonstrate the potential of the reduced order cable element in solving a challenging application. A three-dimensional model of a pantograph/catenary system shown in Figures 12 and 13 is investigated. The model includes the horizontal zigzag course of the contact wire as well as the lateral motion of the catenary. The data for the catenary and pantograph are provided in Tables 3 and 4. Similar parameters were chosen as for the two-dimensional model based on a second order Bernoulli–Euler beam theory studied by Teichelmann et al. [23]. The droppers are modelled by non-linear springs without compression force and with damping. No stitch wires are included, thus the critical speed is expected to be quite low. The simulation started with the pantograph at the beginning of the cable and

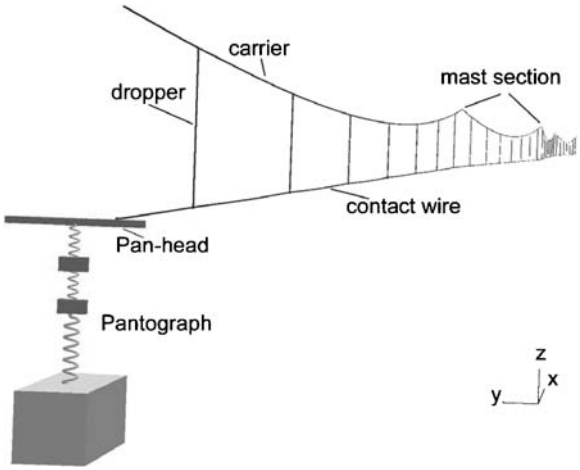

Figure 13. Three-dimensional pantograph/catenary system.

the pantograph and catenary were in static equilibrium, such that the catenary shows no initial dynamic displacement and the contact force at the pantograph is $F_{\mathrm{H}} = 100\,\mathrm{N}$. Figure 14 shows the contact force between catenary and pantograph for two different velocities of the pantograph. The high oscillatory content of the contact forces are reflected in this example, as known from the literature, see e.g. Poetsch et al. [8]. In order to exclude tension forces in the sliding joint presented earlier, the constraint force perpendicular to the contact plane is excluded. While the zigzag course of the wire (alternating at each mast section) does not significantly influence the overall contact force, a three-dimensional model of the catenary system can show interesting dynamics in the case of curved tracks, track switches or side wind. The integration of the catenary and the pantograph in one multibody system allows for the analysis of more sophisticated pantograph/catenary models, such as models that employ a controlled contact force.

Table 3. Data for the catenary system.

Total length	240 m
Mast sections	4
Droppers per section	7
Maximum height of mast	1.5 m
Dropper EA	1.342×10^6 N
Dropper EI	1.5 Nm^2
Dropper ρA	0.089 kg/m
Carrier EA	1.342×10^7 N
Carrier EI	150 Nm^2
Carrier ρA	0.446 kg/m
Contact wire EA	1.342×10^7 N
Contact wire EI	150 Nm^2
Contact wire ρA	0.89 kg/m
Zigzag maximum displacement	0.3 m
Damping wires β	0.03 N s/m^2
Damping dropper	8 N s/m
Gravity	9.81 m/s^2
No. of elements in contact wire	224

Table 4. Data for the pantograph.

Masses (kg)	
M_1	6.4
M_2	7.2
M_3	4.8
Spring constants (N/m)	
c_1	4700
c_2	13,912
c_3	80
Damping constants (N s/m)	
d_1	50
d_2	15
d_3	85
Vertical force at M_1 (N)	
F_H	100

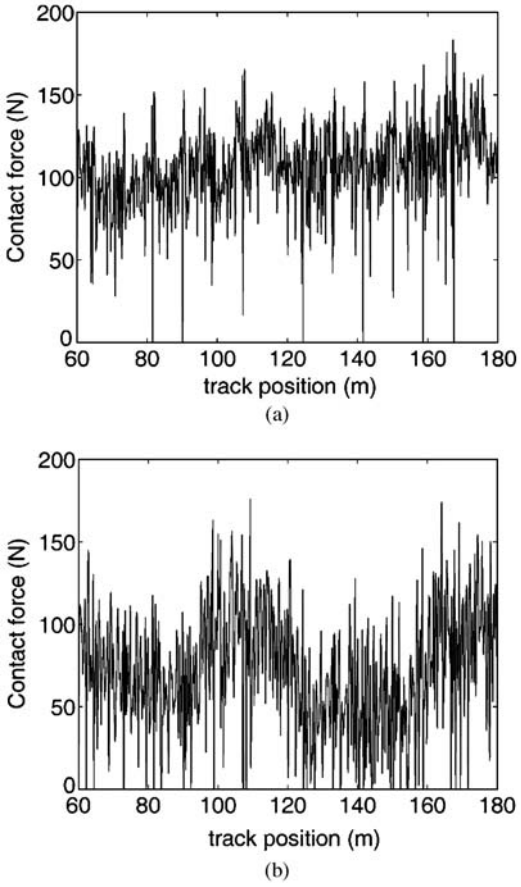

Figure 14. Contact force at pan-head for 32 m/s (a) and 45 m/s (b).

8. Conclusions

The performance of the absolute nodal co-ordinate formulation in the case of thin and stiff structures is investigated in this paper. The results obtained using elements previously reported in the literature are compared with the results of other elements based on cubic interpolation. A higher order element based on the absolute nodal co-ordinate formulation was introduced. This element does not suffer from locking and has better convergence characteristics in the case of thin beams. A lower order cable element is also examined and it is shown that such an element is more efficient for cable problems as compared to the original element. Several stiff and thin beam examples that can be used for future comparisons by other researchers are presented.

Appendix A

In this appendix, the definition of the curvature used in this paper is presented. In this definition, the curvature is expressed in terms of derivatives with respect to the x co-ordinate of the beam instead of derivatives with respect to the curve length s. To this end, the Seret–Frenet frame is defined using the following unit vectors:

$$\mathbf{i} = \mathbf{r}_s, \quad \mathbf{j} = \frac{\mathbf{r}_{ss}}{|\mathbf{r}_{ss}|}, \quad \mathbf{k} = \mathbf{i} \times \mathbf{j} \tag{A-1}$$

where $\mathbf{r}$ is the position vector of an arbitrary point on the beam centreline. The curvature is defined as

$$\kappa = |\mathbf{r}_{ss}| \tag{A-2}$$

The third expression in Equation (A-1) leads to

$$|\mathbf{i} \times \mathbf{j}| = \left| \mathbf{r}_s \times \frac{\mathbf{r}_{ss}}{|\mathbf{r}_{ss}|} \right| = 1. \tag{A-3}$$

Note that $\mathbf{r}_s = \mathbf{r}_x \frac{dx}{ds}$ and since $\mathbf{r}_s = \frac{\mathbf{r}_x}{|\mathbf{r}_x|}$, one has $\frac{dx}{ds} = \frac{1}{|\mathbf{r}_x|}$. It follows that

$$\mathbf{r}_{ss} = \frac{d}{ds}\left(\frac{\mathbf{r}_x}{|\mathbf{r}_x|}\right) = \frac{\mathbf{r}_{xx}}{|\mathbf{r}_x|}\frac{dx}{ds} + \mathbf{r}_x \frac{d}{ds}\left(\frac{1}{|\mathbf{r}_x|}\right) = \frac{\mathbf{r}_{xx}}{(|\mathbf{r}_x|)^2} + \mathbf{r}_x \frac{d}{ds}\left(\frac{1}{|\mathbf{r}_x|}\right). \tag{A-4}$$

Since $\mathbf{r}_s$ is a unit vector, the curvature in Equation (A-2) can be written on utilizing the preceding equation as

$$\kappa = |\mathbf{r}_s \times \mathbf{r}_{ss}| = \left| \frac{\mathbf{r}_x}{|\mathbf{r}_x|} \times \left(\frac{\mathbf{r}_{xx}}{|\mathbf{r}_x|^2} + \mathbf{r}_x \frac{d}{ds}\left(\frac{1}{|\mathbf{r}_x|}\right)\right)\right| = \frac{|\mathbf{r}_x \times \mathbf{r}_{xx}|}{|\mathbf{r}_x|^3} \tag{A-5}$$

which is the definition of the curvature used in this paper and previously used by Dmitrochenko and Pogorelov [11].

Appendix B

The following appendix presents the closed form expressions for the variation of the axial strain and curvature for the cable element. The variation of the axial strain is given by

$$\delta\varepsilon_{xx}^{\mathrm{a}} = \frac{\partial}{\partial e}\left(\frac{1}{2}\left(\mathbf{r}_x^{\mathrm{T}}\mathbf{r}_x - 1\right)\right)\delta\mathbf{e} = \mathbf{r}_x^{\mathrm{T}}\frac{\partial\mathbf{r}_x}{\partial\mathbf{e}}\delta\mathbf{e} = \mathbf{r}_x^{\mathrm{T}}\mathbf{S}_x\delta\mathbf{e}. \tag{B-1}$$

The derivative of the total curvature can be expressed as

$$\frac{\partial\kappa}{\partial e_i} = \frac{\partial}{\partial e_i}\frac{|\mathbf{r}_x\times\mathbf{r}_{xx}|}{|\mathbf{r}_x|^3} = \frac{1}{g^2}\left(g\frac{\partial f}{\partial e_i} - f\frac{\partial g}{\partial e_i}\right) \tag{B-2}$$

with the terms

$$f = |\mathbf{r}_x\times\mathbf{r}_{xx}|, \quad g = |\mathbf{r}_x|^3 \tag{B-3}$$

The variation of the curvature is computed from the partial derivatives of f and g given respectively by:

$$\begin{aligned}\frac{\partial}{\partial e_i}f &= \frac{\partial}{\partial e_i}|\mathbf{r}_x\times\mathbf{r}_{xx}| = \frac{\partial}{\partial e_i}((\mathbf{r}_x\times\mathbf{r}_{xx})^{\mathrm{T}}(\mathbf{r}_x\times\mathbf{r}_{xx}))^{1/2}\\ &= ((\mathbf{r}_x\times\mathbf{r}_{xx})^{\mathrm{T}}(\mathbf{r}_x\times\mathbf{r}_{xx}))^{-1/2}\left((\mathbf{r}_x\times\mathbf{r}_{xx})^{\mathrm{T}}\left(\frac{\partial}{\partial e_i}\mathbf{r}_x\times\mathbf{r}_{xx} + \mathbf{r}_x\times\frac{\partial}{\partial e_i}\mathbf{r}_{xx}\right)\right)\end{aligned} \tag{B-4}$$

$$\frac{\partial}{\partial e_i}g = \frac{\partial}{\partial e_i}\left(\mathbf{r}_x^{\mathrm{T}}\mathbf{r}_x\right)^{3/2} = 3\left(\mathbf{r}_x^{\mathrm{T}}\mathbf{r}_x\right)^{1/2}\left(\mathbf{r}_x^{\mathrm{T}}\frac{\partial\mathbf{r}_x}{\partial e_i}\right). \tag{B-5}$$

The curvature can be computed using a small number of algebraic manipulations by means of pre-computed terms that do not depend on the index i.

Acknowledgments

Support of the author J. Gerstmayr by a APART scholarship, project "Dynamics of Flexible Multibody Systems with Non-Classical Constraints", of the Austrian Academy of Sciences is gratefully acknowledged. This research is also supported in part by the U.S. Army Research Office, Research Triangle Park, NC.

References

1. Shabana, A. A., *Dynamics of Multibody Systems*, 2nd edn., Cambridge University Press, Cambridge, 1998.
2. Ryu, J., Kim, S. S., and Kim, S. S., 'A general approach to stress stiffening effects on flexible multibody dynamic systems', *Mechanics of Structures and Machines* **22**, 1994, 157–180.
3. Rodríguez, J. I., Jiménez, J. M., Funes, F. M., and García de Jalón, J., 'Recursive and residual algorithms for the efficient numerical integration of multi-body systems', *Multibody System Dynamics* **11**, 2004, 295–320.
4. Yakoub, R. Y. and Shabana, A. A., 'Use of Cholesky coordinates and the absolute nodal coordinate formulation in the computer simulation of flexible multibody systems', *Nonlinear Dynamics* **20**, 1999, 267–282.

5. Gerstmayr, J., 'The absolute coordinate formulation with reduced strain for the efficient simulation of flexible multibody systems with nonlinear constraints', in *Proceedings of the ECCOMAS 2004*, P. Neittaanmäki, T. Rossi, S. Korotov, E. Oñate, J. Périaux, and D. Knörzer (eds.), Jyväskylä, Helsinki, 2004.
6. Shabana, A. A., Hussien, H. A., and Escalona, J. L., 'Application of the absolute nodal coordinate formulation to large rotation and large deformation problems', *ASME Journal of Mechanical Design* **120**, 1998, 188–195.
7. Buckham, B., Driscoll, F. R., and Nahon, M., 'Development of a finite element cable model for use in low-tension dynamics simulation', *Journal of Applied Mechanics* **71**, 2004, 476–485.
8. Poetsch, G., Evans, J., Meisinger, R., Kortuem, W., Baldauf, W., Veitl, A., and Wallaschek, J., 'Pantograph/catenary dynamics and control', *Vehicle System Dynamics* **28**, 1997, 159–195.
9. Sugiyama, H. and Shabana, A. A., 'Use of plasticity theory in flexible multibody system dynamics', in *Proceedings of DETC'03 ASME Design Engineering Technical Conferences*, Chicago, IL, 2003, Paper No. VIB-48326.
10. Sopanen, J. T. and Mikkola, A. M., 'Description of elastic forces in absolute nodal coordinate formulation', *Nonlinear Dynamics* **34**, 2003, 53–74.
11. Dmitrochenko, O. N. and Pogorelov, D. Y., 'Generalization of plate finite elements for absolute nodal coordinate formulation', *Multibody System Dynamics* **10**, 2003, 17–43.
12. Von Dombrowski, S., 'Analysis of large flexible body deformation in multibody systems using absolute coordinates', *Multibody System Dynamics* **8**, 2002, 409–432.
13. Yakoub, R. Y. and Shabana, A. A., 'Three dimensional absolute nodal coordinate formulation for beam elements', *ASME Journal of Mechanical Design* **123**, 2001, 606–621.
14. Simo, J. C. and Vu Quoc, L., 'On the dynamics of flexible beams under large overall motions, the plane case. Part I', *Journal of Applied Mechanics* **53**, 1986, 849–863.
15. Bathe, K.-J., *Finite Element Procedures in Engineering Analysis*, Prentice-Hall, Englewood Cliffs, NJ, 1982.
16. Braess, D., *Finite Elements – Theory, Fast Solvers, and Applications in Solid Mechanics*, Cambridge University Press, Cambridge, 1997.
17. Sugiyama, H., Gerstmayr, J., and Shabana, A. A., 'Deformation modes of the finite element cross section', Technical Report MBS05-2-UIC, Department of Mechanical Engineering, University of Illinois at Chicago, 2005.
18. Simo, J. C. and Rifai, M. S., 'A class of mixed assumed strain methods and the method of incompatible modes', *International Journal for Numerical Methods in Engineering* **29**, 1990, 1595–1638.
19. Rade, L. and Westergren, B., *Mathematics Handbook for Science and Engineering*, 4th edn., Springer-Verlag, Berlin Heidelberg, 1999.
20. Sugiyama, H., Escalona, J. L., and Shabana, A. A., 'Formulation of three-dimensional joint constraints using the absolute nodal coordinates', *Nonlinear Dynamics* **31**, 2003, 167–195.
21. Wu, S. C. and Haug, E. J., 'Geometric non-linear substructuring for dynamics of flexible mechanical systems', *International Journal for Numerical Methods in Engineering* **26**, 1988, 2211–2226.
22. Muñoz, J. J. and Jelenić, G., 'Sliding contact conditions using the master–slave approach with application on geometrically non-linear beams', *International Journal of Solids and Structure* **41**, 2004, 6963–6992.
23. Teichelmann, G., Schaub, M., and Simeon, B., 'Modelling and simulation of railway cable systems', *Zeitschrift für Angewandte Mathematik und Mechanik* **85**(12), 2005, 864–877.
24. Schwab, A. L. and Meijaard, J. P., Proceedings of IDETC/CIE 2005 ASME 2005 International Design Engineering Technical Conferences & Computers and Information in Engineering Conference 2005, Long Beach, California, USA. Paper No. DETC2005-85104.